Journal of Materials Chemistry A

PAPER

View Article Online
View Journal | View Issue

Cite this: J. Mater. Chem. A, 2019, 7, 23989

Single-phase Ni_5P_4–copper foam superhydrophilic and aerophobic core–shell nanostructures for efficient hydrogen evolution reaction†

Manisha Das, Nityasagar Jena, Taniya Purkait, Navpreet Kamboj, Abir De Sarkar and Ramendra Sundar Dey *

The facile synthesis of a highly durable, low-cost and robust electrocatalyst for hydrogen generation from water is vital to address the existing environmental issues, as well as to provide an environmentally-friendly clean and green energy supply. Electrochemical deposition of single-phase nickel phosphide on galvanostatically deposited copper foam (Cuf@Ni_5P_4) core–shell nanostructure offers an innovation in the structural design of a new platform for novel electrocatalysts. The Cuf@Ni_5P_4 provides a superior three-dimensional conductive channel for ion transport during the catalytic process. The catalyst exhibits an excellent electrocatalytic activity towards the hydrogen evolution reaction (HER) in acidic media. The superhydrophilic and aerophobic properties of the porous electrode help the H_2 gas bubbles to quickly leave the surface. Interestingly, it requires a very low overpotential of 90 mV for HER at a current density of 10 mA cm^{-2}. The very small Tafel slope of 49 mV dec^{-1} and the very high exchange current density (~0.76 mA cm^{-2}) originate from the large electrochemically active surface area and the fast mass and electron transfer efficiency of the Cuf@Ni_5P_4 catalyst. A theoretical study was performed to investigate the mechanism underlying the HER activity in Cu-supported Ni_5P_4 at an atomic scale. Density functional theory (DFT) calculations suggest a very high negative Gibbs free energy change (ΔG_{H^*}) in Ni_5P_4 (0001)/Cu (111) upon hydrogen adsorption, which is actually responsible for the excellent HER activity of the catalyst. Furthermore, it shows remarkable durability for hydrogen generation under low (10 mA cm^{-2}) and high current densities (160 mA cm^{-2}) for >84 h with ~96% retention of the overpotential, establishing a low-cost and efficient catalyst for sustainable, future energy generation strategies.

Received 24th June 2019
Accepted 2nd August 2019

DOI: 10.1039/c9ta06729a

rsc.li/materials-a

Introduction

The electrochemical generation of H_2 from water has attracted considerable attention, as it is one of the promising approaches used for the production of renewable fuels aimed at future energy supply. Hydrogen generation is economically favorable and environmentally friendly as it generally gives pure products, which are free from CO.[1,2] In addition, not only is H_2 required as the starting material for fuel cells, several industries also have a demand for it as a precursor material for the production of ammonia and the refining of petroleum. To date, several catalysts for the hydrogen evolution reaction (HER) have been developed, among them, noble metal catalysts such as platinum for HER are recognized as benchmark catalysts owing to their high efficiency and low overpotential towards electrocatalytic reactions.[2,3] However, due to limited resources and the expense of noble metal catalysts, transition metal (Ni, Co, Fe and Mn)-based catalysts have drawn attention owing to their performance and their abundant sources.

Transition metal sulfides, phosphides and selenides are the most studied catalysts and have drawn enormous attention in recent years.[4] Typically phosphorous-based transition metal pnictide with the earth abundant element nickel, and nickel phosphides have gained considerable attention as HER catalysts owing to their high activity and stability.[5–8] Nickel phosphide exists in several phases in nanostructures such as Ni_3P, Ni_2P, Ni_5P_2, Ni_5P_4, NiP_2 and $Ni_{12}P_5$.[9] Ni_2P was theoretically predicted to be an efficient HER electrocatalyst, even better than Pt,[10] and experimental validation has been carried out by several researchers.[1,11–15] Recently, Ni_5P_4 crystalline nanoparticles have been explored to produce H_2 in acidic media.[6,16,17] Although most of the mixed phased nickel phosphides are reported to have a good electrocatalytic activity towards HER, they also have some disadvantages such as uncontrolled agglomeration, less hydrophilicity and poor contact resistance which stop them from being used in commercial applications.[18] Single-phase Ni_5P_4 has been proven to show better electrode kinetics than

Institute of Nano Science and Technology (INST), Mohali-160064, Punjab, India. E-mail: rsdey@inst.ac.in

† Electronic supplementary information (ESI) available. See DOI: 10.1039/c9ta06729a

the multiphase nickel phosphides during catalysis. Pan *et al.* successfully synthesized single phase NiP_2, $Ni_{12}P_5$ and Ni_5P_4, and showed that the single phase Ni_5P_4 was the best electrode material in terms of the HER among the other nickel phosphide based catalysts.[5] This is owed to the amount of positive charge on the Ni ($Ni^{\delta+}$) in Ni_5P_4, which is greater than the other nickel phosphides, this helps to achieve better catalytic performances. However, the synthesis of single-phase Ni_5P_4 is still a challenge to researchers in this field.

Strategic synthetic approaches and stepwise routes have been employed to create rational active sites to achieve the superior catalytic activity of nickel phosphide.[13] Several procedures have recently been explored such as hydrothermal, high temperature reactions and wet chemical routes/hydrothermal in combination with a high temperature reaction and an electrochemical method for the synthesis of nanostructured nickel phosphide catalysts.[4] However, to the best of our knowledge, to date an electrochemical synthesis of a single-phase nickel phosphide has not been reported, for instance crystalline Ni_5P_4, for the HER. Electrochemical synthesis has several advantages over other methods, such as: (i) the electrochemical reaction is usually a one-step process; (ii) it does not involve a high temperature for the phosphorization reaction; (iii) the reaction time is reduced; and (iv) self-supported catalyst loading is possible on the electrode surface. It has been established that a rough electrode surface is known to favor the electrodeposition of the desired material.[19] Furthermore, an electrodeposited core–shell material offers a synergistic effect between the core and shell that results in the high efficiency of the nanostructures.[20,21] Electrodeposited porous architectures have the advantages of creating a hydrophilic as well as a aerophobic surface, which helps to decrease the ohmic resistance of the electrode with electrolyte and the fast removal of gas bubbles from the surface.[22] Herein, taking advantage of these effects, for the first time, we have explored the single-phase electrochemical synthesis of nickel phosphide (Ni_5P_4) on a galvanostatically deposited copper foam (Cuf) electrode. The dendritic nanostructure of Cuf offers a rough surface and acts as template for the deposition of Ni_5P_4. The core–shell morphology of Cuf@Ni_5P_4 further shows an excellent catalytic activity towards the HER in acidic medium.

Dr Ramendra Sundar Dey is a Scientist at the Institute of Nano Science and Technology, Mohali, India. Prior to this, he was a Hans C. Ørsted postdoc fellow at the Technical University of Denmark (DTU), Denmark. He received a PhD in Chemistry in 2013 from the Indian Institute of Technology (IIT) Kharagpur, India. Over the past 6 years he has been involved in research in the field of electroanalytical chemistry and nanotechnology. His current research is focused on the architecture and engineering of carbonaceous materials for advanced energy storage technology and non-novel metal catalysts for hybrid energy systems. Dr Dey has published more than 25 research articles, three book chapters and filed many patents. He has been honoured with a number of prestigious National and International awards.

Experimental

Preparation of copper foam electrode

The Cuf thin film was grown on Cu foil using the galvanostatic electrodeposition method following our previous report with a few modifications.[23] First, a copper foil (0.5×0.5 cm^2) was cleaned with dilute nitric acid followed by deionized (DI) water repeatedly and finally with ethanol. The Cu foil was kept in an argon atmosphere when not in use to avoid atmospheric oxidation. The deposition of Cuf was carried out using a two-electrode deposition process, in which the copper foil was used as both the cathode and anode with a fixed distance of 1.5 cm. A constant current density of 1 A cm^{-2} was applied between the electrodes placed in an electrochemical cell containing 0.4 M $CuSO_4$ in 1.5 M H_2SO_4 for a duration of 45 s. The as-deposited Cuf was washed in DI water 3–4 times to remove any acidic residue and kept in an argon atmosphere for further use.

Electrodeposition of Ni_5P_4 on copper foam

Electrodeposition of Ni_5P_4 on the Cuf was carried out under a constant potential of −0.8 V in a three-electrode system. Typically, electrodeposition was carried out in an aqueous solution of $NiCl_2 \cdot 6H_2O$ (60 mM), $NaH_2PO_2 \cdot H_2O$ (50 mM), and NaH_2PO_4 (0.5 M) for different periods of time (30, 60, 90 and 120 min). Previously deposited Cuf was used as a working electrode, platinum wire as the counter electrode, and Ag/AgCl (3 M KCl) as the reference electrode for all of the depositions. The as-deposited black layer of nickel phosphide (Fig. S1†) on Cuf thin film was washed thoroughly with Millipore water and stored under a vacuum when not in use.

Electrodeposition of Ni_5P_4 on different substrates. For comparison of the catalytic activity, the electrodeposition of Ni_5P_4 on different substrates such as copper foil (Ni_5P_4/Cu foil), graphite plate (Ni_5P_4/GP) and nickel foam (Ni_5P_4/Nif) were carried out in a three-electrode system at a constant potential of −0.8 V. Prior to the electrodeposition, the substrates were cleaned using their required method. All other conditions were kept the same as the previous section for the electrodeposition of Ni_5P_4 on different substrates.

Electrode fabrication with Pt/C

A glassy carbon (GC) (2 mm diameter) electrode was cleaned with alumina powder as mentioned earlier for the preparation of Pt/C. Homogeneous ink was prepared using commercially available Pt/C (20 wt%) and was dispersed in a mixed solution of water and ethanol (1 : 1, v/v) and followed by sonication for

30 min. The ink was further drop casted onto the GC electrode for Pt/C to obtain a mass loading of 0.5 mg cm^{-2}.

Electrochemical measurements

All of the electrochemical characterization measurements for the HER were conducted at room temperature (25 °C) with Cuf@Ni_5P_4 (0.5 × 0.5 cm^2) as the working electrode, Ag/AgCl (3 M KCl) and the graphite rod were used as the reference and counter electrode, respectively. All of the linear sweep voltammetry (LSV) and cyclic voltammetry (CV) experiments were carried out to check the HER activity with 0.5 M H_2SO_4 as the electrolyte. All of the potentials used in this study were calibrated to a reversible hydrogen electrode (RHE) based on the formula

$$E_{RHE} = (E_{Ag/AgCl(3\ M\ KCl)} + 0.210 + 0.0591\ pH)V$$

The chronopotentiometric (CP) measurements were conducted to evaluate the durability of the as-prepared electrocatalyst under the same experimental conditions without compensating the *iR* drop. Commercial Pt/C catalysts were employed for hydrogen evolution, respectively, as the baseline catalysts for comparison. Electrochemical impedance spectroscopy (EIS) measurements were carried out at a potential of −0.2 V (*vs.* RHE) in the frequency range of 10^5–10^{-2} Hz. The polarization curves for all of the catalysts were *iR* corrected (unless mentioned otherwise) to minimize the effect of the ohmic resistance present at the electrode electrolyte interface and the current was normalized with the geometrical surface area. The *iR*-correction was performed according to the following equation:

$$E_{corr} = E_{mea} - iR_s$$

in which E_{corr} is the *iR*-corrected potential, the E_{mea} is the experimentally measured potential, and R_s is the equivalent series resistance extracted from the Nyquist plots at the open circuit potential.

Computational methodology

Density functional theory (DFT) calculations were performed within the Vienna *ab initio* simulation package (VASP).[24] The ion-electron exchange correlation functionals were treated with the projector augmented wave (PAW)[25,26] pseudopotentials by considering the Perdew–Burke–Ernzerhof (PBE)[27] parametrization form of the generalized gradient approximation (GGA) with a kinetic energy cutoff of 500 eV to expand the electronic wave functions in a plane wave basis-set. A *Γ*-centered 5 × 5 × 1 k – mesh was used for the Brillouin zone (BZ) sampling with an energy threshold of 1×10^{-5} eV for the total energy convergence and a force tolerance of 0.01 eV $Å^{-1}$ for the ionic and electronic relaxation. The periodic replicas of the slab geometry were decoupled by considering a large vacuum spacing of more than 20 Å along the *z*-axis. In addition, the van der Waals (vdW) corrections to the dispersive forces were explicitly treated using the Grimme DFT-D2 method for the surface adsorbed geometries.

Results and discussion

Characterization of the electrode materials

The core–shell Cuf@Ni_5P_4 thin film electrode (Fig. S1, ESI†) was synthesized by the electrodeposition method in a three-electrode system at a constant potential of −0.8 V, which is schematically shown in Fig. 1 (details are given in the experimental section). The growth of Ni_5P_4 at different deposition times (30, 60, 90 and 120 min) was performed with the aim of achieving the best electrocatalytic activity of Cuf@Ni_5P_4 and the optimized time was found to be 90 min. All of the characterizations were conducted using Cuf@Ni_5P_4 prepared under the optimal conditions (*i.e.* a deposition time of 90 min). The structural analysis was investigated using X-ray powder diffraction (XRD) analysis. Fig. 2a and b displays the XRD pattern of Cuf@Ni_5P_4, in which all of the diffraction peaks are in good agreement with the hexagonal structure of Ni_5P_4 (JCPDS PDF 01-089-2588). The diffraction peaks at the 2*θ* values of 28.69°, 32.57°, 36.06°, 41.42°, 47.06°, 47.84°, 52.96°, 53.98°, 57.74°, 61.06°, 69.66°, 76.46° and 79.01° were attributed to the planes of (103), (004), (104), (211), (300), (301), (214), (220), (304), (107), (320), (226) and (413), respectively for Ni_5P_4. However, the diffraction peaks for bare Cuf at a 2*θ* of 43.19°, 50.30° and 73.89° correspond to the (111), (200) and (220) planes, respectively, for the cubic lattice (JCPDS PDF 01-070-3038), which were also observed as expected in the diffraction pattern of Cuf@ Ni_5P_4. However, the peaks of Cuf@Ni_5P_4 were observed to be shifted by an angle of approximately 0.3° with respect to the peak for bare Cuf towards a lower angle of 2*θ* owing to the uniform interfacial strain induced in the geometry of the core and shell which originated from the strong size mismatch between them.[28,29] This confirms the interfacial interaction of the hybrid core–shell nanostructure formed during electrochemical synthesis.[30] The two small peaks are observed at a 2*θ* of 37.24° and 38.95°, which corresponds to the (111) plane of NiO (PDF 00-047-1049) and the (111) plane of CuO (PDF 00-001-1117), respectively. The peak arising for CuO may be due to the exposure of the sample to the air atmosphere and the appearance of a small oxide peak of nickel (NiO) may be due to its formation in the working electrolyte conditions during the electrodeposition process.[31,32] The selected area electron diffraction (SAED) pattern obtained during the transmission electron microscopic (TEM) measurement (Fig. 2c), again reveals the single-phase Ni_5P_4 formation on Cuf, which is well correlated with the XRD pattern.

The surface morphological information for the as-deposited Cuf and Cuf@Ni_5P_4 was systematically investigated using scanning electron microscopy (SEM) and TEM. The SEM images of Cuf (Fig. 3a and S2, ESI†) show the honeycomb porous structure resulting from the generation and dissipation of H_2 bubbles during the electrodeposition process.[33] The SEM images of Cuf@Ni_5P_4 at different deposition durations demonstrate the growth of Ni_5P_4 with time (Fig. S3, ESI†). Cuf@Ni_5P_4 shows a similar structure to Cuf with uniformly

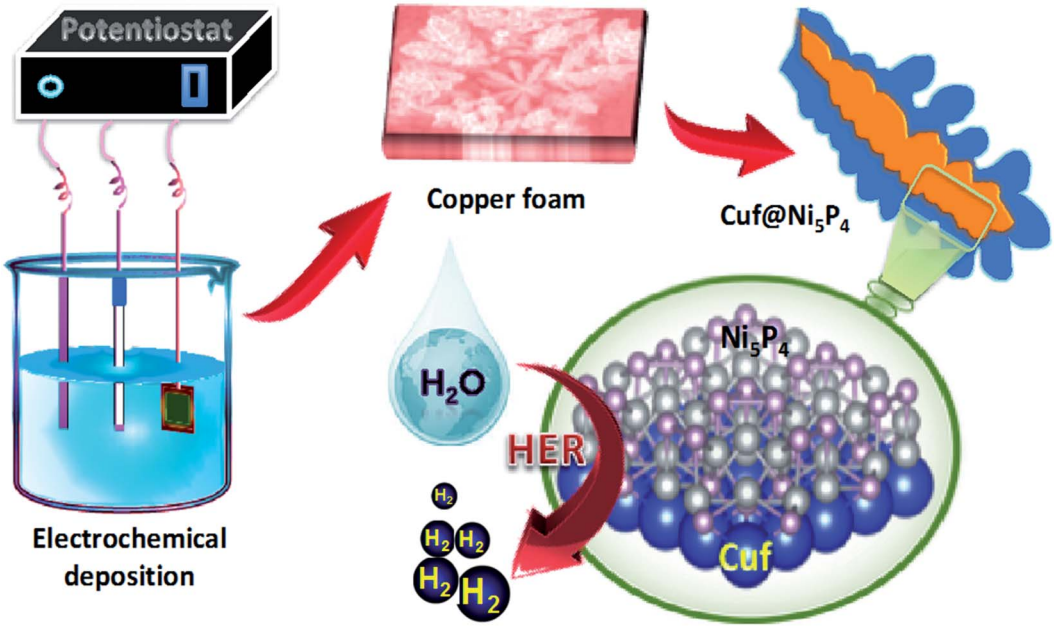

Fig. 1 Schematic illustration of the electrochemical synthesis of the copper foam-nickel phosphide active material and the HER activity.

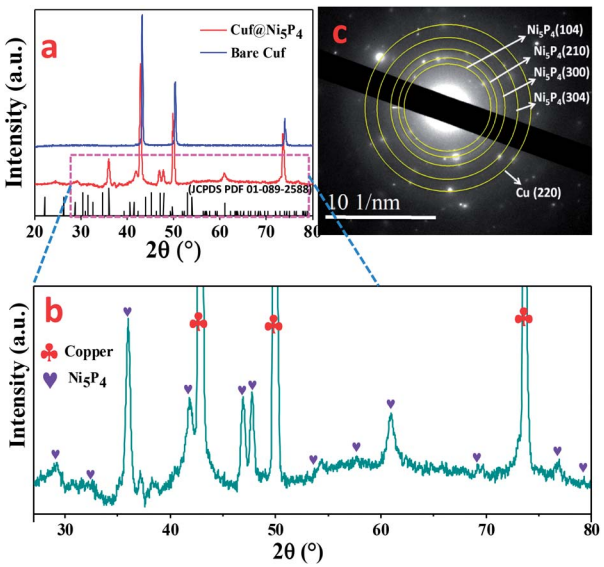

Fig. 2 (a) XRD pattern for Cuf (blue) and Cuf@Ni_5P_4 (red); (b) scaled image of XRD of Cuf@Ni_5P_4; and (c) SAED pattern for Cuf@Ni_5P_4.

distributed continuous macropores across the surface (Fig. 3b and S4, ESI†). Unlike Cuf@Ni_5P_4, the SEM images of the electrodeposited Ni_5P_4/GP, Ni_5P_4/Cu foil and the Ni_5P_4/Nif samples are particulate in nature (Fig. S5, ESI†). Although they have different morphologies, all of the materials exhibit aggregated particles throughout the surface. The pore size distribution (Fig. S6, ESI†) reveals that the average pore size of the bare Cuf was approximately 110 μm, which was reduced to an average pore size of approximately 85 μm in the Cuf@Ni_5P_4, which indicates the deposition of Ni_5P_4 is *via* the electrodeposition technique. The high-resolution SEM images at different magnifications, (Fig. 3c and d) further suggests the formation of a dendritic Ni_5P_4 film onto the copper foam.

The TEM images of the Cuf@Ni_5P_4 (Fig. 3e and S7a and b, ESI†) show the dendritic structure of the material. A close look at Fig. 3e and f shows the different intensities of the layer, which arise from the transmission dependency of the different atomic layers as schematically represented in Fig. 3g. The thickness of the deposited layer calculated from the high-resolution TEM (HRTEM) image was 30–40 nm (Fig. 3f) with a core diameter of 0.4–0.8 μm which proves the formation of a core shell nanostructure with copper as the core and Ni_5P_4 as the shell. This hierarchically structured electrode with a core–shell configuration is known to show excellent electrocatalytic activity towards hydrogen generation.[21] The HRTEM study was performed with the Ni_5P_4 material as the shell (Fig. 3h). Well-resolved lattice fringes were observed with *d*-spacing values of 0.222, 0.248 and 0.217 nm, which correspond to the (210), (104) and (211) planes of Ni_5P_4, respectively. The junction of the core–shell heterostructures, as revealed from the HRTEM images shown in Fig. 3i and j, indicate the presence of the (001) plane of Ni_5P_4, grown on the copper (111) plane. The energy dispersive X-ray spectra (EDX) suggests the presence of Ni, Cu and P elements in the sample (Fig. S8, ESI†). The EDX mapping study was accomplished over a branched structure of Cuf@Ni_5P_4 (Fig. 3k–n). The EDX elemental mapping study proves the homogeneous distribution of the nickel, phosphorous and copper elements on the branched structure. It is noteworthy from the mapping analysis that the more intense red (for Ni) and blue (for P) color at the branched structure and the green color (for Cu) throughout the scanned area further confirm that the Ni_5P_4 thin film fully covered the Cuf nanostructure. The surface area, pore volume and pore size were analysed using the Brunauer–Emmett–Teller (BET) method using N_2 adsorption–desorption

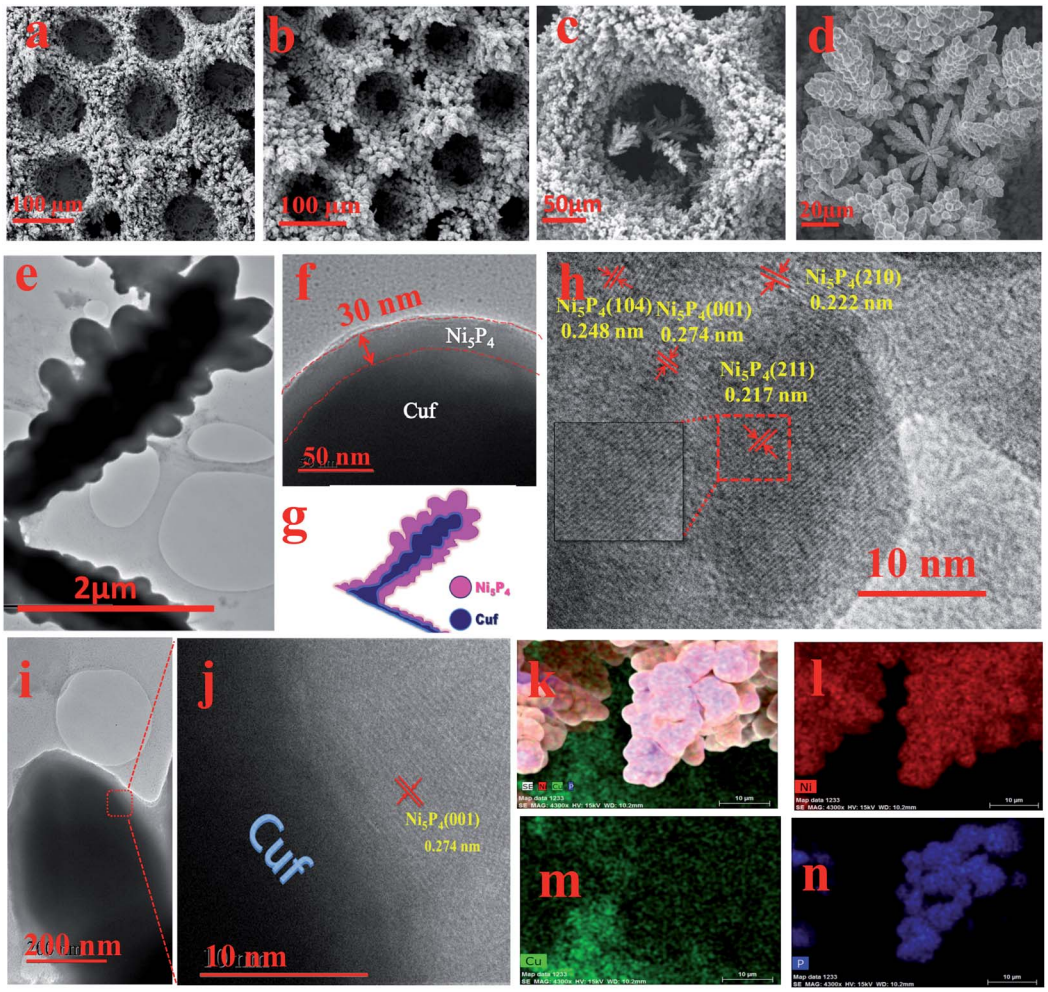

Fig. 3 (a) SEM image of bare Cuf; (b–d) SEM images of Cuf@Ni_5P_4 at different magnifications; (e) and (f) TEM images of Cuf@Ni_5P_4 reflecting the core shell nanostructure of the catalyst; (g) schematic illustration showing the core–shell nanostructure of Cuf@Ni_5P_4; (h) high resolution TEM image of Cuf@Ni_5P_4 (inset shows an enlarged version of the selected area from the HRTEM image); (i and j) HRTEM images of the interface of Cuf@Ni_5P_4 showing the (001) plane of Ni_5P_4 present at the interface; and (k–n) elemental mapping of Cuf@Ni_5P_4.

isotherms (Fig. S9a, ESI†). The specific surface area of our material, Cuf@Ni_5P_4, was found to be 6.944 m^2 g^{-1}. The isotherms were type IV, which are usually identified for mesoporous materials. The average pore size was found to be 9.29 nm (Fig. S9b, ESI†), which plays a part in the efficient catalytic activity of the catalyst.

X-ray photoelectron spectroscopy (XPS) is an important tool to ascertain the chemical states of the elements present in a sample. As shown in Fig. 4a, the XPS survey scan confirms the presence of Ni, Cu, P, C as well as O elements. The presence of C and O can be attributed to the surface adsorbed electrolyte ion or surface oxidation of the material.[11] The high-resolution XPS spectra of Ni 2P were employed to detect the metallic and oxidized peak corresponding to Ni $2P_{3/2}$ and Ni $2p_{1/2}$ (Fig. 4b). Interestingly, two metallic peaks for Ni ($Ni^{\delta+}$) corresponding to 853.4 and 870.3 eV were identified.[34,35] The spectrum of Ni 2P also indicates the presence of peaks at 856.8 (oxidized Ni) and 862.3 eV (satellite) for Ni $2p_{3/2}$ and at 875.6 (oxidized Ni) and 880.2 eV (satellite) for the Ni $2p_{1/2}$ energy level.[5] The high-

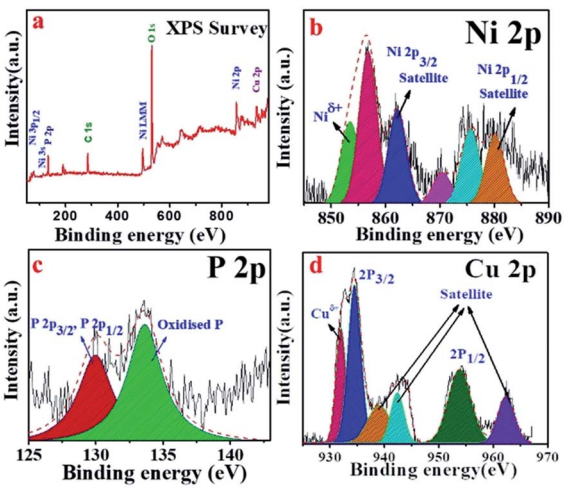

Fig. 4 (a) XPS survey spectra of Cuf@Ni_5P_4, and high-resolution deconvoluted XPS sspectra for: (b) Ni 2p; (c) P 2p; and (d) Cu 2p.

resolution spectrum of P 2p for the Cuf@Ni_5P_4, in which the peak at 129.9 eV was assigned to the P $2p_{3/2}$ and P $2p_{1/2}$, whereas the peak at 133.4 eV was attributed to the oxidized P species (Fig. 4c). The XPS spectra of copper present as a core in Cuf@Ni_5P_4 (Fig. 4d), indicates three main peaks at 932.1, 934.5, and 953.7 eV, which are attributed to metallic Cu ($Cu^{\delta+}$), Cu $2p_{3/2}$ (oxidized Cu) and Cu $2p_{1/2}$ (oxidized Cu), respectively. The three peaks which appeared at a binding energy of 939.1, 942.4, and 962.4 eV were attributed to the satellite peaks of the Cu $2p_{3/2}$ and $2p_{1/2}$, respectively.[36,37]

Electrochemical characterization

The electrocatalytic activity of the as-prepared catalyst was evaluated by means of the HER in 0.5 M H_2SO_4. There are only a few reports in the literature of a single-phase synthesis of Ni_5P_4 used for the generation of H_2.[16,18] However, all of the reports either failed to achieve a high exchange current density or did not perform for a long time in acidic medium. In order to assess the electrocatalytic activity of the as-prepared Cuf@Ni_5P_4, a systematic electrochemical characterization for HER was performed. All of the potential used here was converted to the RHE unless mentioned otherwise. The polarization curve of the electrodeposited nickel phosphide on Cuf at different deposition durations (Fig. S10, ESI†), clearly shows that a 90 min deposition time gives the best HER activity in terms of the overpotential and chemical kinetics. As observed from the SEM images (Fig. S3, ESI†), more coverage of electrodeposited Ni_5P_4 films is obtained with a deposition time of up to 90 min. Further deposition (120 min) inhibits the charge transfer between the Cuf and Ni_5P_4, which weakens the catalytic performances of the electrode. Fig. 5a displays the obtained polarization curve for Pt/C, Cuf@Ni_5P_4, Ni_5P_4/GP, Ni_5P_4/Cu foil, Ni_5P_4/Nif and bare Cuf at a scan rate of 10 mV s^{-1}. The Cuf@Ni_5P_4 catalyst attained an overpotential (η) of 90 mV at a current density of 10 mA cm^{-2}, which is 239 mV more positive than bare Cuf, 148 mV more positive than Ni_5P_4/GP, 113 mV more positive than Ni_5P_4/Cu foil, 36 mV more positive than Ni_5P_4/Nif and 63 mV more negative in comparison to Pt/C. Interestingly, the Cuf@Ni_5P_4 catalyst displays a η of only 164 mV even at a very high current density of 100 mA cm^{-2}. It is noteworthy to mention here that the achieved overpotential of Cuf@Ni_5P_4 is very low compared to the previously reported data on nickel phosphide based electrocatalysts (Fig. 5b and Table S1, ESI†).[1,18,38] The excellent electrocatalytic activity of Cuf@Ni_5P_4 reveals the important role of the core shell nanostructures of the catalyst and confirms that the surface nickel phosphide (shell) exploited the copper (core) in terms of the porosity and surface area, resulting in a superior catalytic performance of these a core/shell nanostructures. The HER electrocatalytic activity crucially depends on the uneven electrode surface.[39]

The corresponding Tafel plots were employed to determine the kinetics of the HER rate for the different catalysts (Fig. 5c). The Tafel slope for Cuf@Ni_5P_4 derived from the Tafel plot was found to be 49 mV dec^{-1}, which is less than that of the Ni_5P_4/Cu foil (slope = 93 mV dec^{-1}), Ni_5P_4/GP (110 mV dec^{-1}), Ni_5P_4/Nif (87 mV dec^{-1}) and bare Cuf (150 mV dec^{-1}), which determines the better kinetic rate of Cuf@Ni_5P_4 for hydrogen generation. However, the Tafel slope of Pt/C was found to be 27 mV dec^{-1}.

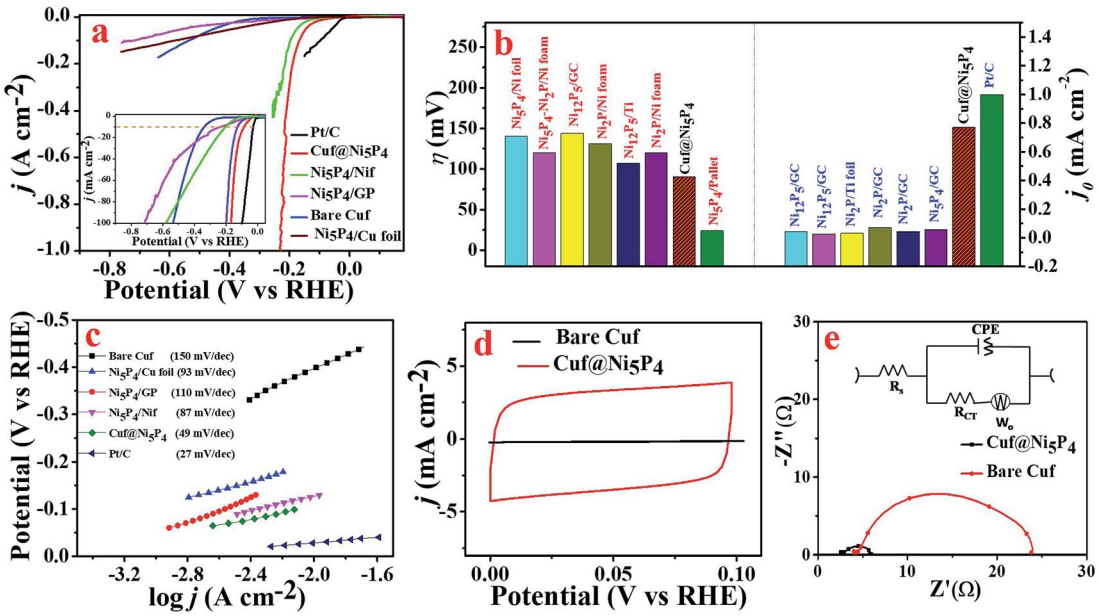

Fig. 5 (a) HER polarization curves for bare Cuf, Ni_5P_4/Cu foil, Ni_5P_4/GP, Ni_5P_4/Nif, Cuf@Ni_5P_4 and Pt/C catalysts recorded at a scan rate of 10 mV s^{-1}. (b) Bar diagram depicting the comparison of the overpotential and the exchange current density of the previously reported nickel phosphide based electrocatalyst. (c) Tafel plots of bare Cuf, Ni_5P_4/Cu foil, Ni_5P_4/GP, Ni_5P_4/Nif, Cuf@Ni_5P_4 and Pt/C. (d) CV response of bare Cuf and Cuf@Ni_5P_4 at a scan rate of 100 mV s^{-1}. (e) Nyquist plot of bare Cuf and Cuf@Ni_5P_4 recorded at −0.2 V (*vs.* RHE), the inset shows the equivalent circuit used to fit the EIS data. All of the experiments were performed in 0.5 M H_2SO_4 solution.

An electrode with a larger exchange current density needs less driving force (smaller current density) to conduct the HER.[40] The exchange current density of Cuf@Ni_5P_4 was calculated to be 0.76 mA cm^{-2} by extrapolating the linear part of the Tafel plot to the *X*-axis and it was found to be very close to that of the exchange current density of Pt/C (1.00 mA cm^{-2}) in 0.5 M H_2SO_4 (Fig. S11, ESI†). The exchange current density achieved by Cuf@Ni_5P_4 was the highest in comparison with the recently reported nickel phosphide based electrocatalysts[38,41–43] (Table S2, ESI†). The exchange current density is usually expressed in terms of the projected or geometric surface area and depends on the surface roughness or roughness factor (RF) of the catalyst.[37] The porous nature of the nanostructure offers a high electrochemically active surface area (ECSA) and leads to more electrochemically active sites that undoubtedly help to improve the electrocatalytic activity.[44] A comparative CV scan was performed to calculate the ECSA and RF of Cuf@Ni_5P_4 (Fig. 5d). The CV response obtained from Cuf@Ni_5P_4 at different scan rates in a non-faradic region (0 to 0.1 V) and the corresponding scan rate *versus* the anodic and cathodic peak current for the calculation of the value of the double layer capacitance (C_{dl}) are shown Fig. S12 (ESI†). The ECSA was calculated and found to be 423.5 cm^2 by considering the C_{dl} of 33.9 mF cm^{-2} and the specific capacitance (C_{sp} = 0.02 mF cm^{-2}) of the Ni surface in the 0.5 M H_2SO_4 electrolyte.[45] The RF was calculated to be 1694 (see ESI† for details), which is very high and outperforms the state-of-the-art catalysts reported to date.[46–50]

To study the electrode kinetics (charge transfer behavior), EIS of the bare Cuf and Cuf@Ni_5P_4 (Fig. 5e) were recorded at −0.2 V (*vs.* RHE). An equivalent circuit model was employed to fit the Nyquist plot as shown in the inset of Fig. 5e. Interestingly, Cuf@Ni_5P_4 possesses a very small solution resistance (R_s = 2.59 Ω) which indicates a reduced interfacial resistance and the superior catalytic activity of the as-prepared catalyst. The charge transfer resistance (R_{ct}) of Cuf@Ni_5P_4 was only 3.62 Ω (giving rise to the rapid charge transfer kinetics), which is much lower than that of bare Cuf (R_{ct} = 20 Ω). The EIS of the nickel phosphide deposited on Cuf for different periods of time (Fig. S13, ESI†), clearly indicates that the minimum R_{ct} of Cuf@Ni_5P_4 with a 90 min deposition time was obtained as compared to the other catalyst. The low R_s and R_{ct} value of Cuf@Ni_5P_4 ensures the fast charge transfer kinetics between the catalyst and the electrolyte, as well as the catalyst to the electrode, which facilitates the faster reaction rate. It is generally accepted that small values of R_s correspond to close contact between the current collector and catalysts.

During the catalytic process, plenty of bubbles are generated from the surface of the electrode which blocks electrolyte diffusion and increases the ohmic resistance between the electrode and the electrolyte interfaces, which decreases the ECSA and eventually leads to degradation of the catalytic performance. To overcome this challenge, it is necessary to design a fine surface catalyst which is hydrophilic as well as aerophobic in nature.[51] To understand the hydrophilicity of the as-synthesized catalyst, wettability analysis on the surface of the Cuf@Ni_5P_4 electrode was performed by measuring the contact angle of the water drop on the surface of the catalyst. Fig. 6a shows that the droplet imposes no contact with the surface of Cuf@Ni_5P_4 and when the drop falls on the surface, the Cuf@Ni_5P_4 catalyst absorbed the liquid drop instantly (Fig. 6b) with a contact angle of 0°, indicating that the material is superhydrophilic in nature. An aerophobic study of the catalyst was also performed by analysing the bubble formation during and after the LSV run, demonstrated in Fig. 6c–e. The aerophobic nature of the foam-like Cuf@Ni_5P_4 core–shell nanostructure provides an abrupt renewal of the gas bubbles (as schematically shown in the bottom panel of Fig. 6),[52] which helps to increase the efficiency of the catalyst towards hydrogen evolution. When the HER process has just started the average size of the bubbles formed on the surface were approximately 200 μm at an overpotential of approximately 60 mV and the size starts to increase and is observed to be approximately 300 μm at an overpotential of approximately 130 mV, which is due to the rapid renewal of the minor gas bubbles. Interestingly, when the LSV was stopped it was observed that only a few bubbles, which were trapped in the pores, were seen resembling the superior aerophobic behavior of the catalyst. The superhydrophilic and aerophobic nature of the sample originated from the fine nanostructures and selection of an appropriate material is crucial for HER electrocatalysis.

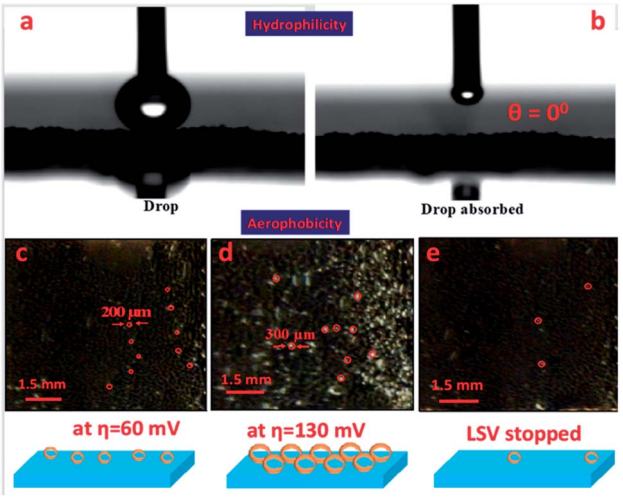

Fig. 6 Wettability test of the Cuf@Ni_5P_4 surface: (a) before; and (b) after placing a liquid drop with a contact angle of 0°. (c–e) Optical images with a schematic diagram in the bottom panel showing the bubble formation behavior on the Cuf@Ni_5P_4 surface at different overpotentials and at the end of LSV.

To ascertain the origin of the high electrocatalytic activity in the as-synthesized materials and to deepen the understanding of the HER mechanism, DFT calculations were performed. As established, the electrochemical reduction of ionic hydrogen on a metal-catalyst surface is a combination of a hydrogen adsorption process called the Volmer reaction step followed by either the Tafel or Heyrovsky reaction mechanism for H_2 desorption (see ESI† for details). The H* (in which * refers to atomic hydrogen over the surface of the catalyst) is the rate determining step for proton adsorption in an acidic medium. To estimate the hydrogen adsorption energy ($E_{Ads.}$) and the

ΔG_{H^*} of the reaction intermediate, H*, different metal-catalyst surfaces were explored using the computational hydrogen electrode model proposed by Nørskov *et al.*[53] as follows:

$$\Delta G_{H^*} = E_{Ads.} + \Delta E_{ZPE} - T\Delta S$$

$$E_{Ads.} = E_{surface+H} - E_{surface} - 1/2E_{H_2}$$

in which $E_{Ads.}$ is the hydrogen adsorption energy on the surface of the metal catalyst, $E_{surface+H}$ and $E_{surface}$ are the total ground state energy of H adsorbed surface and the pure metal catalyst surface, whereas E_{H_2} is the energy of the H_2 molecule in the vacuum gas-phase state. ΔE_{ZPE} and ΔS are the zero-point energy and entropy difference between the adsorbed state (H*) and molecular gas-phase state of hydrogen (H_2), and T is the absolute temperature (T = 298.15 K in our calculation). The zero-point energy (E_{ZPE}) of the H exposed surfaces was evaluated from the harmonic vibrational frequencies at 0 K. The entropy of the H adsorbed surfaces was found to be very small in our calculation (Table S3, ESI†) and hence, can be safely ignored by assuming the entropy of the H_2 molecule is $\Delta S = -1/2\Delta S(H_2) = -64.915$ J mol^{-1} K^{-1} in the standard gas phase state at a pressure of 1 bar, temperature 300 K and pH = 0.

In order to explore the HER activity of the pure Ni_5P_4 (0001) and Ni_5P_4 (0001)/Cu (111) hybrid catalyst surface, several hydrogen adsorption sites around the surface Ni and P atoms in the optimized geometry of the Ni_5P_4 (0001) surface (Fig. S14, ESI†) have been considered to rule out the most probable ones.

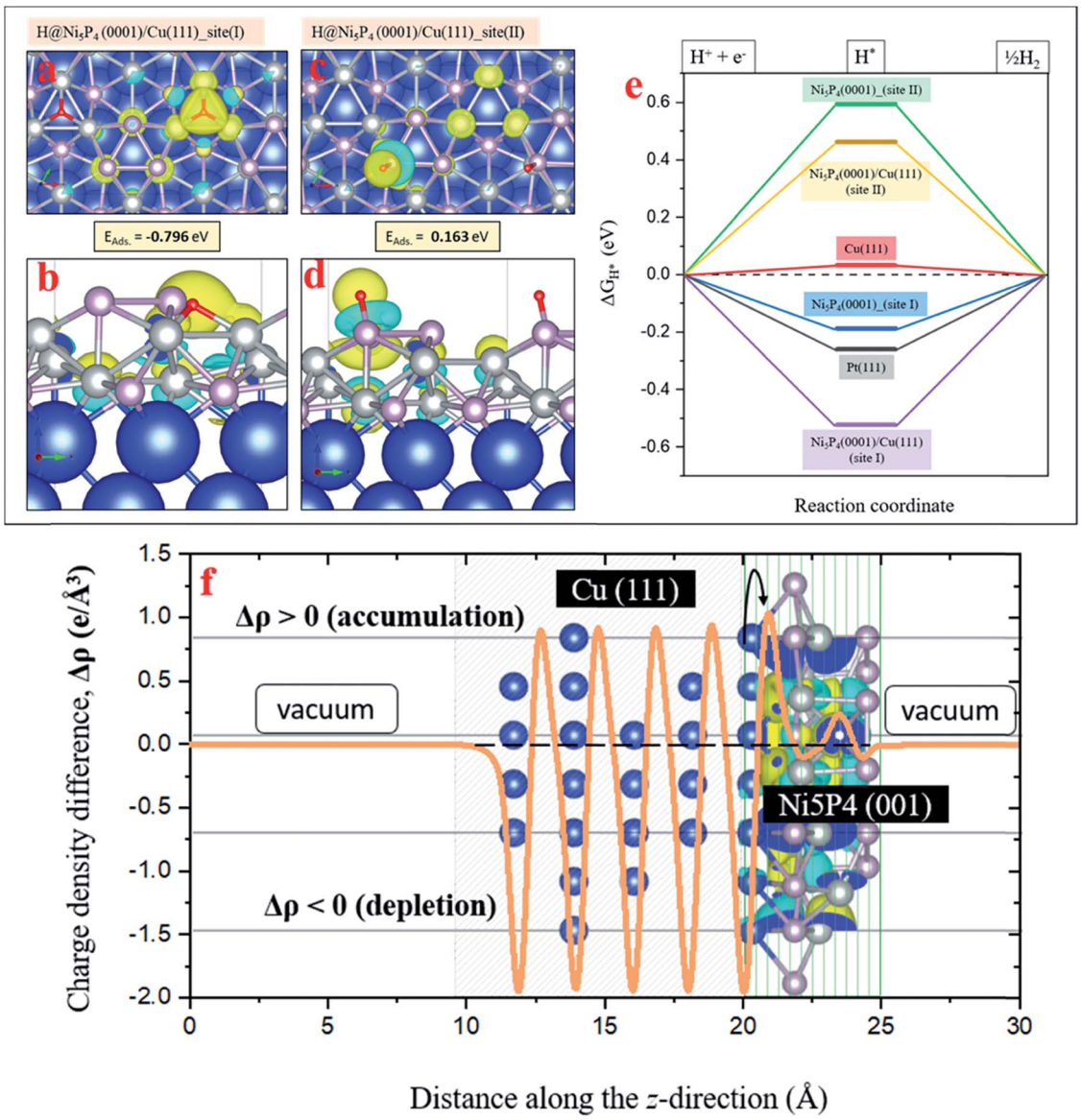

Fig. 7 (a and b) A top and side view of H* adsorption over the three-fold Ni site of the Ni_5P_4 (0001)/Cu (111) (site I). (c and d) H* over the on-top P site of the Ni_5P_4 (0001)/Cu (111) surface (site II). The differential ground state charge density distribution around the adsorbate (H*) is at an isolevel of 0.59×10^{-2} e Å^{-3}. (e) The ΔG_{H^*} of the reaction intermediate (H*) on different metal-catalyst surfaces (f) Charge density difference and charge transfer at the interface between Cu (111) and Ni_5P_4 (001) surface.

As demonstrated in Fig. 3i and j, the (001) plane of Ni_5P_4 is present at the Cuf@Ni_5P_4 interface. Fig. S15 in ESI† describes how the three-fold Ni hollow site (site I) and the on-top P site (site II) turn out to be the two most favorable hydrogen adsorption sites with binding energies of −0.54 eV and 0.21 eV, respectively. These adsorption sites have been used for further studies on the Ni_5P_4 (0001)/Cu (111) hybrid interface structure with the Cu (111) surface underneath the Ni_5P_4 (0001) surface. Fig. 7a and b shows the adsorption geometry of H* on the three-fold Ni site (site I) of Ni_5P_4 (0001)/Cu (111) with a binding energy of −0.79 eV, which is the highest among all of the surfaces explored in this study, indicating the importance of Cuf support in facilitating the HER activity in the Ni_5P_4 nanostructures. Similar to the hydrogen adsorption over the on-top P site (site II) of Ni_5P_4 (0001), the interface structure of Ni_5P_4 (0001)/Cu (111) also exhibits a positive H binding energy of 0.16 eV with a strong delocalization of the valence charge density around the P atom, as shown in Fig. 7c and d. Details of the H* adsorption on various metal-catalyst surfaces and computational details have been provided in the ESI (Fig. S15, S16, and Table S3, ESI†).

The change in the Gibbs free energy (ΔG_{H^*}) of the reaction intermediate, for example H*, is a well-known descriptor of the HER activity of any adsorbate ($1/2E_{H_2}$ in this case) over a metal-catalyst surface. According to the Sabatier principle, a good catalyst should have a ΔG_{H^*} value as close as possible to 0 eV. The ΔG_{H^*} of the reaction intermediate H* on different metal-catalyst surfaces was measured. The Ni_5P_4 (0001) and Ni_5P_4 (0001)/Cu (111) surface with H* adsorbed over the three-fold Ni site (site I) exhibited a negative value of ΔG_{H^*}, favoring the HER activity (Fig. 7e). In addition, the negative value of ΔG_{H^*} was found to be much higher (−0.52 eV) for the Ni_5P_4 (0001)/Cu (111) surface as compared to the value of −0.18 eV for the Ni_5P_4 (0001) surface. This is attributable to a very high negative adsorption energy, $E_{Ads.} = -0.79$ eV of H* over the Ni_5P_4 (0001)/Cu (111) surface and a localized charge density distribution around the three-fold Ni site of the adsorbate, which strongly binds the atomic hydrogen to its surface (Fig. 7a and b). While for H* at the on-top P site of Ni_5P_4 (0001) and the Ni_5P_4 (0001)/Cu (111) surface, a very high positive value of ΔG_{H^*} indicates a much weaker binding of H* or a reduction in the desorption of hydrogen, resulting in a much lower HER activity. The adsorption geometry of H* on the three-fold Ni site (site I) of Ni_5P_4 (0001)/Cu (111) with a binding energy of −0.79 eV, which is the highest among all of the surfaces explored in this study, indicates the importance of Cuf for the deposition of Ni_5P_4 nanostructures towards HER activity. The high value of the H-binding energy results from the charge transfer between Cu (111) and Ni_5P_4 (0001), as the interface is chemical in nature. The interfacial study of the Cuf@Ni_5P_4 was validated by the interfacial charge density distribution. The interface between Cu and Ni_5P_4 was found to be chemical in nature as shown in Fig. 7f. The charges accumulating at the Cuf@Ni_5P_4 interface are transferred from the portion of the Cu (111) surface, which in turn, becomes depleted. The difference in the charge density distribution was calculated *via* $\Delta\rho = \rho$[interface system] − ρ[Cu (111)] − ρ[Ni_5P_4 (001)]. This calculation is based on the explicit inclusion of the vDW-D3 dispersive interactive forces, which accounts for the long range electronic interactions in the surface geometries.

The electrochemical stability or durability of the catalyst in the working electrolyte is an important parameter that one should look for in a catalyst. The chronopotentiometry test was performed to check the durability of the Cuf@Ni_5P_4 catalyst at a low (10 mA cm^{-2}) as well as high current density (160 mA cm^{-2}) in 0.5 M H_2SO_4 for 84 h. As demonstrated in Fig. 8a, the electrocatalyst showed an excellent stability performance with approximately 96% retention of the overpotential even at a high current density of 160 mA cm^{-2}. The LSV pattern of the Cuf@Ni_5P_4 catalyst was recorded before and after the chronoamperometry study and found a minute change in the overpotential as shown in Fig. 8b, which indicates the excellent durability of the catalyst. In order to check the structural integrity of the catalyst during the stability test, SEM (Fig. 8a, inset) as well as elemental mapping analysis (Fig. S17, ESI†) were performed before and after the chronoamperometry test. The SEM study confirmed the morphology of the catalyst is not altered upon continuous evolution (84 h) of hydrogen gas. Elemental mapping further revealed the presence of Ni, Cu and P even after 84 h of the chronoamperometry test, which proved the structural integrity and superior durability of the Cuf@Ni_5P_4 catalyst. The ultrathin deposited layer (30 nm) of the catalyst on the Cuf could increase the contact area between them and thus decrease the average stress suffered by the hosts upon H_2 generation ensuring excellent structural integrity

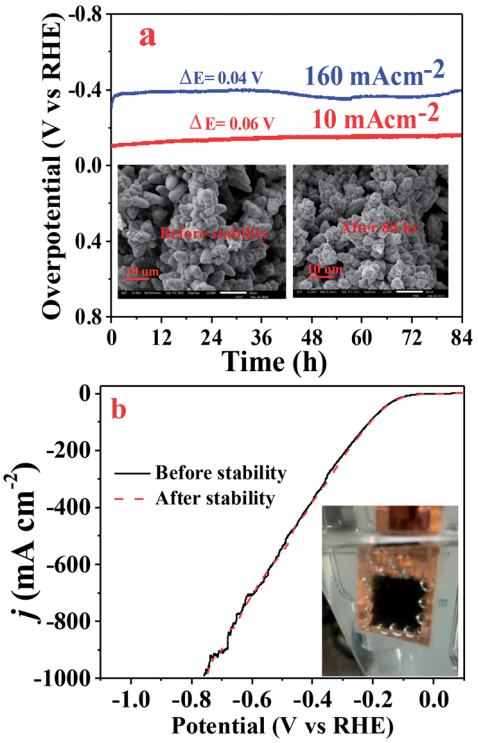

Fig. 8 (a) Chronopotentiometric curve of Cuf@Ni_5P_4 at a current density of 10 and 160 mA cm^{-2}, inset shows the SEM images obtained before and after the test. (b) LSV of Cuf@Ni_5P_4 before and after the chronopotentiometric test.

during continuous gas evolution by the as-prepared catalyst. The excellent durability, along with the outstanding catalytic activity of the catalyst, opens up a new method for the electrochemical generation of hydrogen.

Conclusions

In summary, we present here a simple electrochemical approach to design a single-phase Ni_5P_4 catalyst deposited on a galvanostatically-grown Cuf nanoarchitecture. The core–shell Cuf@Ni_5P_4 catalyst showed a high catalytic activity towards HER in acidic medium with a significantly reduced overpotential and a superior exchange current density. The high ECSA and excessive RF that originates from the foam-like surface of Cuf is essentially responsible for the high electrocatalytic activity of the catalyst. DFT calculations elucidated the origin of a very high negative ΔG_{H^*} in Ni_5P_4 (0001)/Cu (111) upon hydrogen adsorption. This arises owing to a localized charge density distribution around the three-fold Ni site of the adsorbate, which is favorable for the HER activity of the catalyst. The superhydrophilic and aerophobic nanostructured surface actually helps by reducing the contact resistance and the fast release of air bubbles during the catalysis process. Moreover, the Cuf@Ni_5P_4 catalyst shows a long-term durability of 84 h measured using a chronopotentiometry test at a low and high current density with approximately 96% retention of the initial overpotential and preserving the structural consistency, which strongly indicates the superiority of the catalyst. This study opens up a new route for the synthesis of efficient and robust catalysts for the generation of H_2 in a cost-effective and less time-consuming pathway, which will have encouraging future applications in the field of renewable energy.

Conflicts of interest

There are no conflicts to declare.

Acknowledgements

MD acknowledges SERB EMR and INST, Mohali for providing fellowship. This work was financially supported by the DST SERB EMR (EMR/2016/000040) and DST INSPIRE (DST/INSPIRE/04/2015/000337) funding agencies. The authors acknowledge INST, Mohali for instrumental support. Our sincere thanks are extended to CDAC, Pune's supercomputing resources on PARAM YUVA II for the theoretical calculations.

Notes and references

1 X. Wang, Y. V. Kolen'Ko, X. Q. Bao, K. Kovnir and L. Liu, *Angew. Chem., Int. Ed.*, 2015, **54**, 8188–8192.
2 X. Wang, W. Li, D. Xiong, D. Y. Petrovykh and L. Liu, *Adv. Funct. Mater.*, 2016, **26**, 4067–4077.
3 P. W. Menezes, A. Indra, C. Das, C. Walter, C. Göbel, V. Gutkin, D. Schmeißer and M. Driess, *ACS Catal.*, 2017, **7**, 103–109.
4 S. Anantharaj, S. R. Ede, K. Sakthikumar, K. Karthick, S. Mishra and S. Kundu, *ACS Catal.*, 2016, **6**, 8069–8097.
5 Y. Pan, Y. Liu, J. Zhao, K. Yang, J. Liang, D. Liu, W. Hu, D. Liu, Y. Liu and C. Liu, *J. Mater. Chem. A*, 2015, **3**, 1656–1665.
6 J. Li, J. Li, X. Zhou, Z. Xia, W. Gao, Y. Ma and Y. Qu, *ACS Appl. Mater. Interfaces*, 2016, **8**, 10826–10834.
7 A. Han, H. Chen, Z. Sun, J. Xu and P. Du, *Chem. Commun.*, 2015, **51**, 11626–11629.
8 D. Li, K. Senevirathne, L. Aquilina and S. L. Brock, *Inorg. Chem.*, 2015, **54**, 7968–7975.
9 I. K. Mishra, H. Zhou, J. Sun, F. Qin, K. Dahal, J. Bao, S. Chen and Z. Ren, *Energy Environ. Sci.*, 2018, **11**, 2246–2252.
10 P. Liu and J. A. Rodriguez, *J. Am. Chem. Soc.*, 2005, **127**, 14871–14878.
11 P. Wang, Z. Pu, Y. Li, L. Wu, Z. Tu, M. Jiang, Z. Kou, I. S. Amiinu and S. Mu, *ACS Appl. Mater. Interfaces*, 2017, **9**, 26001–26007.
12 C. Du, M. Shang, J. Mao and W. Song, *J. Mater. Chem. A*, 2017, **5**, 15940–15949.
13 X. Xiao, D. Huang, Y. Fu, M. Wen, X. Jiang, X. Lv, M. Li, L. Gao, S. Liu, M. Wang, C. Zhao and Y. Shen, *ACS Appl. Mater. Interfaces*, 2018, **10**, 4689–4696.
14 B. You, N. Jiang, M. Sheng, M. W. Bhushan and Y. Sun, *ACS Catal.*, 2016, **6**, 714–721.
15 J. Xu, J. P. S. Sousa, N. E. Mordvinova, J. D. Costa, D. Y. Petrovykh, K. Kovnir, O. I. Lebedev and Y. V. Kolen'Ko, *ACS Catal.*, 2018, **8**, 2595–2600.
16 A. B. Laursen, K. R. Patraju, M. J. Whitaker, M. Retuerto, T. Sarkar, N. Yao, K. V. Ramanujachary, M. Greenblatt and G. C. Dismukes, *Energy Environ. Sci.*, 2015, **8**, 1027–1034.
17 C. Lai, X. Liu, Y. Deng, H. Yang, H. Jiang, Z. Xiao and T. Liang, *Inorg. Chem. Commun.*, 2018, **97**, 98–102.
18 M. Ledendecker, S. Krick Calderón, C. Papp, H.-P. Steinrück, M. Antonietti and M. Shalom, *Angew. Chem., Int. Ed.*, 2015, **54**, 12361–12365.
19 N. A. C. Hirst, in *The Energy Conundrum*, World Scientific (Europe), 2018, pp. 119–190.
20 S. J. Hwang, S. J. Yoo, J. Shin, Y.-H. Cho, J. H. Jang, E. Cho, Y. Sung, S. W. Nam, T. Lim, S. Lee and S. Kim, *Sci. Rep.*, 2013, **3**, 1309.
21 M. B. Gawande, A. Goswami, T. Asefa, H. Guo, A. V. Biradar, D. Peng, R. Zboril and R. S. Varma, *Chem. Soc. Rev.*, 2015, **44**, 7540–7590.
22 Z. Lu, W. Zhu, X. Yu, H. Zhang, Y. Li, X. Sun, X. Wang, H. Wang, J. Wang, J. Luo, X. Lei and L. Jiang, *Adv. Mater.*, 2014, **26**, 2683–2687.
23 T. Purkait, G. Singh, D. Kumar, M. Singh and R. S. Dey, *Sci. Rep.*, 2018, **8**, 640.
24 G. Kresse and J. Furthmüller, *Phys. Rev. B: Condens. Matter Mater. Phys.*, 1996, **54**, 11169–11186.
25 P. E. Blöchl, *Phys. Rev. B: Condens. Matter Mater. Phys.*, 1994, **50**, 17953–17979.
26 D. Joubert, *Phys. Rev. B: Condens. Matter Mater. Phys.*, 1999, **59**, 1758–1775.
27 J. P. Perdew, K. Burke and M. Ernzerhof, *Phys. Rev. Lett.*, 1996, **77**, 3865–3868.

28 B. D. Cullity and S. R. Stock, *Elements of X-ray Diffraction*, 2nd edn, 1978.
29 I. Meunier, G. Tréglia, J.-M. Gay, B. Aufray and B. Legrand, *Phys. Rev. B: Condens. Matter Mater. Phys.*, 1999, **59**, 10910–10917.
30 S. Shao, J. Shao, H. He and Z. Fan, *Opt. Lett.*, 2005, **30**, 2119.
31 K. Neuróhr, L. Pogány, B. G. Tóth, Á. Révész, I. Bakonyi and L. Péter, *J. Electrochem. Soc.*, 2015, **162**, D256–D264.
32 X. Ma, Y. Chang, Z. Zhang and J. Tang, *J. Mater. Chem. A*, 2018, **6**, 2100–2106.
33 R. S. Dey, H. A. Hjuler and Q. Chi, *J. Mater. Chem. A*, 2015, **3**, 6324–6329.
34 J. Jiang, C. Wang, W. Li and Q. Yang, *J. Mater. Chem. A*, 2015, **3**, 23345–23351.
35 P. W. Menezes, A. Indra, C. Das, C. Walter and C. Göbel, *ACS Catal.*, 2017, 7(1), 103–109.
36 S. Wei, K. Qi, Z. Jin, J. Cao, W. Zheng, H. Chen and X. Cui, *ACS Omega*, 2016, **1**, 1367–1373.
37 J. Tian, Q. Liu, N. Cheng, A. M. Asiri and X. Sun, *Angew. Chem., Int. Ed.*, 2014, **53**, 9577–9581.
38 Z. Huang, Z. Chen, Z. Chen, C. Lv, H. Meng and C. Zhang, *ACS Nano*, 2014, **8**, 8121–8129.
39 M. H. Suliman, A. Adam, M. N. Siddiqui, Z. H. Yamani and M. Qamar, *Catal. Sci. Technol.*, 2019, **9**, 1497–1503.
40 Y. Pan, Y. Liu, J. Zhao, K. Yang, J. Liang, D. Liu, W. Hu, D. Liu, Y. Liu and C. Liu, *J. Mater. Chem. A*, 2015, **3**, 1656–1665.
41 T. Tian, L. Ai and J. Jiang, *RSC Adv.*, 2015, **5**, 10290–10295.
42 Y. Pan, Y. Liu, J. Zhao, K. Yang, J. Liang, D. Liu, W. Hu, D. Liu, Y. Liu and C. Liu, *J. Mater. Chem. A*, 2015, **3**, 1656–1665.
43 E. J. Popczun, J. R. McKone, C. G. Read, A. J. Biacchi, A. M. Wiltrout, N. S. Lewis and R. E. Schaak, *J. Am. Chem. Soc.*, 2013, **135**, 9267–9270.
44 C. C. Chusuei, M. A. Brookshier and D. W. Goodman, *Langmuir*, 1999, **15**, 2806–2808.
45 C. C. L. McCrory, S. Jung, J. C. Peters and T. F. Jaramillo, *J. Am. Chem. Soc.*, 2013, **135**, 16977–16987.
46 J. Chang, K. Li, Z. Wu, J. Ge, C. Liu and W. Xing, *ACS Appl. Mater. Interfaces*, 2018, **10**, 26303–26311.
47 L. Wei, K. Goh, Ö. Birer, H. E. Karahan, J. Chang, S. Zhai, X. Chen and Y. Chen, *Nanoscale*, 2017, **9**, 4401–4408.
48 J. Chang, K. Li, Z. Wu, J. Ge, C. Liu and W. Xing, *ACS Appl. Mater. Interfaces*, 2018, **10**, 26303–26311.
49 Y. Yang, H. Fei, G. Ruan and J. M. Tour, *Adv. Mater.*, 2015, **27**, 3175–3180.
50 A. Dutta, A. K. Samantara, S. K. Dutta, B. K. Jena and N. Pradhan, *ACS Energy Lett.*, 2016, **1**, 169–174.
51 Y. Shi and B. Zhang, *Chem. Soc. Rev.*, 2016, **45**, 1529–1541.
52 H. Li, S. Chen, Y. Zhang, Q. Zhang, Q. Zhang, X. Jia, L. Gu, X. Sun, L. Song and X. Wang, *Nat. Commun.*, 2018, **9**, 1–12.
53 J. Greeley, T. F. Jaramillo, J. Bonde, I. Chorkendorff and J. K. Nørskov, *Nat. Mater.*, 2006, **5**, 909–913.